**Fig. 4.** Readout of the QD photoluminescence as a function of temperature for a forward bias of 0.5 V and a storage time of 100 ms.

The PL line shapes corresponding to the InAs QDs after a storage time of 100 ms for a range of temperatures between 3 and 130 K are shown (Fig. 4). The integrated PL signal in the temperature range from 10 to 130 K falls off with increasing temperature, and from this data, the measured activation energy for the exciton loss with temperature is ~20 meV. Analysis of the luminescence shift with increasing temperature suggests that the temperature dependence of the band gap, together with thermal evaporation of carriers out of the thinnest QDs in the structure, are responsible for the observed red shift. From the collected signal in Fig. 4, we obtained a rough estimate for the device efficiency of ~$10^{-9}$ at 10 K after storing the information for 100 ms. This number could be improved by loading the excitons while the device is under a negative bias of ~$-3$ V. This will ensure a more efficient transfer of the electrons from the X level in the AlAs into the InAs QDs.

The time dependence of the stored luminescence at low temperature (Fig. 5) for a readout bias of 0.5 V shows a stored luminescence signal decay, $I_s$, which can be fitted to two
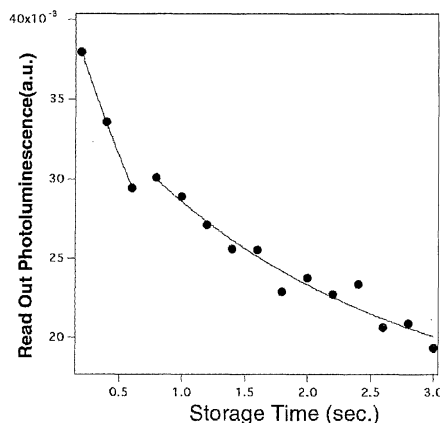


**Fig. 5.** Low-temperature (3 K) integrated intensity of the readout signal as function of time for a forward bias of 0.5 V. The lines are exponential fits to the data. The storage time extrapolated to the average noise level (on this scale, $6 \times 10^{-3}$) is ~10 s.

exponentials. For short storage times (5 μs to 800 ms), $I_s \sim 4 \times 10^{-2}/e^{0.57t}$, but for long storage times (800 ms to 3 s), $I_s \sim 3 \times 10^{-2}/e^{0.18t}$, where $t$ is the storage time in seconds. The stored signal decreases by ~50% in 3 s, and extrapolation to the noise level gives a storage time of nearly 10 s. The origin of these losses is still not clear, but several effects could be responsible for the decreasing readout signal. First, the overlap of the wave functions of electrons and holes could be important, and some of the stored spatially indirect excitons could be lost during the storage time. Second, carrier (hole) losses could occur by capture at deep levels in the AlAs barrier by tunneling during the storage cycle. Third, it is possible that some of the electrons stored in the InAs QDs could be recombining with the residual holes, because the MBE material has a carbon acceptor background concentration of ~$5 \times 10^{15}$ cm$^{-3}$.

The exciton storage times are remarkably long, ~$10^9$ times those of the exciton lifetimes in QDs ($1 - 5 \times 10^{-9}$ s). These long exciton storage times should also be compared to exciton lifetimes in n-doped/insulator/p-doped/insulator QW structures. Typical values of ~1 ms at 4 K have been reported (10), and in this case the structure does not exhibit a memory function. In type I–type II–coupled QW structures that do not contain QDs, exciton lifetimes of a few microseconds have been reported (9). The long storage times in the present QD structures are consistent with electron-hole pair localization in

the QD pairs and a low concentration of recombination centers in the QDs.

Much remains to be done to fully understand these long exciton lifetimes and to make use of the high density of QDs as an inexpensive storage medium. Nevertheless, writing and retrieving information using light and self-assembled QDs may offer substantial speed and power advantages for the next generation of devices.

**References and Notes**
1. J. J. Finley et al., Appl. Phys. Lett. **73**, 2618 (1998).
2. G. Yusa and H. Sakaki, Appl. Phys. Lett. **70**, 345 (1997).
3. C. Rocke et al., Phys. Rev. Lett. **78**, 4099 (1997).
4. A. Wixforth, J. P. Kotthaus, W. Wegscheider, M. Bichler, Science **283**, 1292 (1999).
5. D. Leonard, M. Krishnamurthy, C. M. Reaves, S. P. DenBaars, P. M. Petroff, Appl. Phys. Lett. **63**, 3203 (1993).
6. M. Fricke, A. Lorke, J. P. Kotthaus, G. Medeiros-Ribeiro, P. M. Petroff, Eur. Phys. Lett. **36**, 197 (1996).
7. E. Dekel et al., Phys. Rev. Lett. **80**, 4991 (1998); G. Abstreiter et al., Jpn. J. Appl. Phys. **38**, 449 (1999).
8. W. Schoenfeld, T. Lundstrom, P. M. Petroff, Appl. Phys. Lett. **74**, 2194 (1999).
9. J. Feldmann et al., Solid State Commun. **83**, 245 (1992).
10. W. Rehm, P. Ruden, G. H. Döhler, K. Ploog, Phys. Rev. B **28**, 5937 (1983); G. H. Döhler, in Properties of III-V Superlattices and Quantum Wells, P. Bhattacharya, Ed. (Electronic Materials Information Service, Stevenage, UK, 1996), vol. 15, p. 11.
11. Supported by the U.S. Army Research Office (contract number DAA G56-97-1-1301) and by QUEST, an NSF Science and Technology Center (DMR no. 91-20007).

24 August 1999; accepted 27 October 1999

# Experimental Tunneling Ratchets

H. Linke,[1]* T. E. Humphrey,[1] A. Löfgren,[2] A. O. Sushkov,[1] R. Newbury,[1] R. P. Taylor,[1] P. Omling[2]

Adiabatically rocked electron ratchets, defined by quantum confinement in semiconductor heterostructures, were experimentally studied in a regime where tunneling contributed to the particle flow. The rocking-induced electron flow reverses direction as a function of temperature. This result confirms a recent prediction of fundamentally different behavior of classical versus quantum ratchets. A wave-mechanical model reproduced the temperature-induced current reversal and provides an intuitive explanation.

In the absence of any net macroscopic forces, asymmetric potentials can be used to induce a particle flow when subjected to external fluctuations (1–5). Referred to as ratchets, their operation has been proposed as the underlying physical principle of molecular motors in biological systems (1, 2, 5–7), such as the

[1]School of Physics, University of New South Wales, Sydney 2052, Australia. [2]Division of Solid State Physics, Lund University, Box 118, 221 00 Lund, Sweden.

*To whom correspondence should be addressed. E-mail: hl@phys.unsw.edu.au

myosin-actin system that affects muscle contraction (8, 9). Fluctuation-induced particle current has also been observed in artificial ratchets (10–16). When tunneling contributes to the particle flow in an adiabatically rocked ratchet, it has been predicted that the current direction will depend on temperature (17). Here we use quantum confinement to define an electron ratchet in a semiconductor nanostructure. We find that the two contributions to the rocking-induced current (tunneling through and excitation over the ratchet's energy barrier) flow in opposite directions.

Thus, the net current direction depends on the electron energy distribution at a given temperature. This behavior can be compared to the energy-sorting task assigned to Maxwell's demon, and it also demonstrates a fundamental difference between classical and quantum ratchets (17–19).

A quantum ratchet can be established by confining electrons to an asymmetric conducting channel of a width comparable to the electron wavelength. Shown in the inset of Fig. 1A, the darker regions are etched trenches that laterally confine a two-dimensional sheet of electrons located parallel to the surface of a GaAs/AlGaAs heterostructure. The channel's periodic variation in width induces a corresponding variation in electron confinement energy that creates asymmetric energy barriers at each constriction. When a source-drain bias voltage $U$ is applied, the resulting current $I$ is determined by the barrier's reflection and tunneling coefficients and is sensitive to the precise shape of these barriers. Because of the geometric asymmetry, the electric field along the channel produced by the voltage $U$ deforms the barriers in a way that depends on the polarity of $U$ (Fig. 1B), such that $I(U) \neq -I(-U)$. Thus, a net current $I_{net} = (0.5)[I(U_0) + I(-U_0)]$ is generated when a square-wave source-drain voltage of amplitude $U_0$ is applied, even though the time-averaged electric field is zero. In this way, current is generated in a rocked ratchet, where the term "rocking" refers to the effect of the voltage on the ratchet potential. Here we realize such an electron ratchet in the tunneling regime and experimentally confirm the theoretical prediction (17) that the current direction in quantum ratchets depends on temperature $T$.

Experimental data from two devices are presented. One device, denoted by R10, had a channel featuring 10 periodic ratchet cells (Fig. 1A). The other device, R1, consisted of a single ratchet cell of the same shape and size. The lateral dimensions of the ratchet cells, which were patterned with electron-beam lithography and shallow wet etching, were much smaller than the length scales for elastic (6 μm) and inelastic (>10 μm) scattering at the temperatures and voltages used here (energies $k_B T$ and $|eU| \leq 1$ meV, where $k_B$ is Boltzmann's constant and $e$ is the electron charge). A net current was generated using a square-wave voltage of frequency 191 Hz. In order to enhance sensitivity, the square-wave voltage was 100% amplitude modulated, so that it was effectively applied in periodic bursts (repetition frequency of 17 Hz), and the two-terminal average current $I_{net}$ during each burst was measured by phase locking on the repetition frequency. None of the elements in the path of the current, such as ohmic contacts, caused substantial rectification (20). All of the measurement frequencies were much lower than any electron energy-relaxation processes in the electron gas (<1 ns), so that, electronically, the ratchet was in a stationary state at all times (so-called "adiabatic rocking"). The width of the conducting channel was tuned by using the electron sheet regions parallel to

the channel as side gates. A lower (more negative) side-gate voltage $V_g$ corresponds to a narrower channel and therefore higher potential barriers.

In Fig. 1, we show $I_{net}$ versus $V_g$ for both devices in a range where the conductance of the devices (top axis in Fig. 1, A and B) was of the order of $0.2e^2/h$ for R10 (Fig. 1A) and $2e^2/h$ for device R1 (Fig. 1B) (where $h$ is Planck's constant). This conductance corresponds to the transmission of only the lowest one-dimensional (1D) wave mode over each barrier (21), indicating that the barrier height $V_0$ approximately matches the Fermi energy $\mu_F$ of 11.8 meV. The rocking voltage was $U_0 = 1$ mV in both cases and corresponded to a voltage drop of 0.1 mV over each barrier in device R10 (<1% of $\mu_F$) and a drop of 1 mV in device R1. The net current generated in this way corresponds to ∼1 to 5% rectification of the total current and, at 4 K, was initially positive (22) for low $V_g$ but reversed its direction as the barrier height was reduced (Fig. 1). At 0.4 K, additional structure emerged in the plots of $I_{net}$ versus $V_g$. The current reversed direction several times as the barrier height was varied. We studied $I_{net}(T)$ in more detail by slowly warming the devices at fixed $V_g$ (at the values indicated by lettered arrows in Fig. 1) while recording $I_{net}$ (Fig. 2A). Confirming the prediction (17), the current reverses direction as a function of temperature while all other parameters, including the shape and height of the potential barriers, are kept constant.
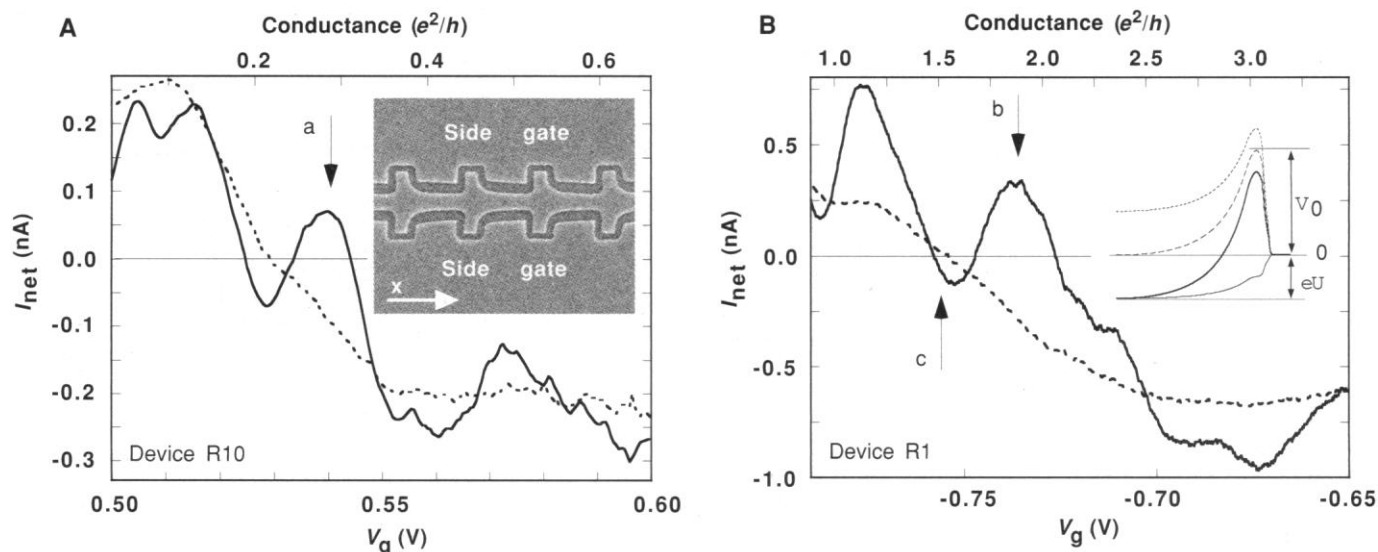


**Fig. 1.** Device description and net current. (**A**) Net current ($U_0 = 1$ mV) versus side-gate voltage $V_g$ (bottom axis) for device R10 at $T = 0.4$ K (solid curve) and 4 K (dotted curve). The top axis is the measured device conductance $G$ as a function of $V_g$. (**Inset**) Scanning electron micrograph of a periodic ratchet, showing four repeated ratchet cells. The channel width is described by $W(x) = \alpha(x - 0.2\ \mu m)^{-1/2} + \beta$ (for 0.21 μm $< x <$ 1.2 μm, repetition period is 1.2 μm), where $\alpha = 0.1\ \mu m^{3/2}$ was defined lithographically and $\beta$ approximates the effect of the side gate. (**B**) Net current for device R1 ($U_0 = 1$ mV) [conditions as in (A)]. Conductance values substantially below $2e^2/h$ (top axis) indicate that transport is in the tunneling regime (21). (**Inset**) The model potential for a single ratchet barrier at positive (bold curve), zero (dashed curve), and negative (dotted curve) bias voltage. The potential was obtained by calculating the energy of the lowest 1D subband $V(x) \approx \hbar^2 k_y(x)^2/2m^*$, where $\hbar$ is $h/2\pi$ and $k_y(x) = \pi/W(x)$ is the lateral $k$ vector in a hard wall potential of shape $W(x)$ for $\beta = -0.083$ μm ($m^* = 0.067 m_e$ is the effective electron mass in GaAs). The result was spatially averaged on a scale of 0.05 μm (yielding $V_0 = 12.0$ meV) to account for smoothing effects in the patterning process visible in the micrograph in (A). The spatial distribution of the voltage drop (thin curve) is constructed so that the gradient is proportional to the gradient of the zero-voltage potential. Points a, b, and c highlight values of $V_g$ where the current direction depends on temperature.

To provide an intuitive understanding of this temperature-induced current reversal, we present a model of 1D transport over a single barrier of a shape based on the geometry of the device (see Fig. 1B). Electron-interference effects inside the individual ratchet cells (13) are not considered here. We assume that the transport is ballistic, no inelastic processes occur, and electrons in all but the lowest subband are fully reflected. Because backscattering is caused by a change in the potential, we assume a spatial distribution of the source-drain voltage drop $eU$ that scales with the local gradient of the zero-voltage potential (Fig. 1B) (13, 23, 24). At low temperatures ($k_B T \ll \mu_F - |eU_0|$), a square-wave voltage of amplitude $U_0$ generates an $I_{net}$ that can be written as (21)

$$I_{net}(\mu_F, U_0, T)$$
$$= -(e/h) \int_0^{\infty} \Delta t(\varepsilon, U_0) \Delta f(\varepsilon, U_0, \mu_F, T) d\varepsilon$$
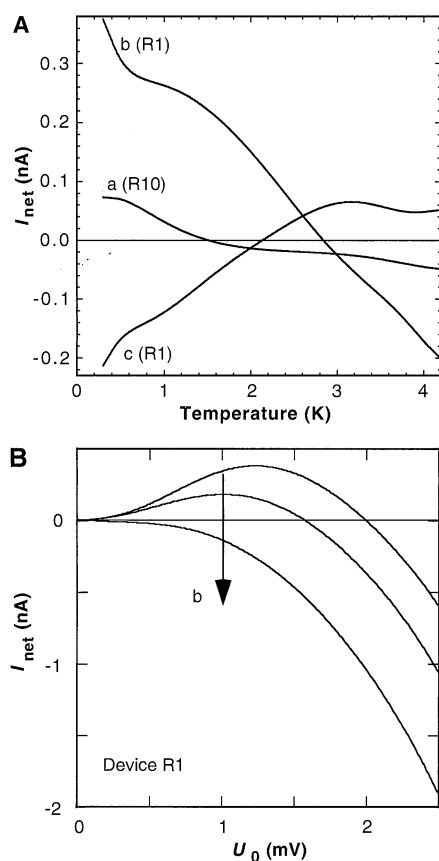
Fig. 2. (A) Temperature-induced current reversal. Net current versus temperature for devices R10 (curve a) and R1 (curves b and c) at fixed gate voltages as indicated by the corresponding letters in Fig. 1. $U_0 = 1$ mV in all cases. The temperature was measured with a calibrated Ge sensor that was heat sunk in the same way as the device. (B) Net current versus rocking amplitude for device R1 at the gate voltage denoted by point b in Fig. 1B at (from top) 0.6, 2, and 4 K.

where $e$, the electron charge, is negative (22). $\Delta f = \{f[\varepsilon + (eU_0/2) - \mu_F, T] - f[\varepsilon - (eU_0/2) - \mu_F, T]\}$ describes the range of the energy $\varepsilon$, in which electrons contribute to the current, and $f(\varepsilon - \mu_F, T)$ denotes the Fermi-Dirac distribution in the electron reservoirs. $\Delta t = \{t[\varepsilon + (eU_0/2), U_0] - t[\varepsilon - (eU_0/2), -U_0]\}$ is the difference between the transmission functions for positive and negative voltages, calculated by numerically solving the 1D time-independent Schrödinger equation. The current is zero in the linear response limit where $\Delta t = 0$.

For $U_0 = 0.5$ mV, we find that $\Delta t(\varepsilon)$ is of the order of $10^{-3}$ for energies within a few millielectron volts of the barrier height $V_0 = 12.0$ meV (Fig. 3). Most important, however, and independent of the exact value of $U_0 < V_0$, $\Delta t$ changes sign as a function of energy. The energy window $\Delta f(\varepsilon)$ is shown in Fig. 3 for $U_0 = 0.5$ mV, $\mu_F = 11.7$ meV, and three different temperatures. At the lowest temperature, the electrons sample an energy region where $\Delta t$ is, on average, positive, resulting in a positive $I_{net}$ at this particular $\mu_F$ and $T$. With increasing $T$, however, more electrons contribute to $I_{net}$ in an energy range where $\Delta t$ is negative. Thus, $I_{net}$ reverses sign as a function of $T$ (solid curve in the lower inset of Fig. 3). Temperature and rocking voltage have a similar energy-averaging effect, such that the temperature at which the current reversal occurs decreases with increasing voltage (Fig. 3, lower inset). This effect is also apparent in Fig. 2B, where $I_{net}$ in device R1 at $V_g = -0.735$ V (point b in Fig. 1B) is shown as a function of the rocking voltage $U_0$ at different temperatures.

The crucial property of the model that leads to the current reversal is the sign change of $\Delta t(\varepsilon)$ around $\varepsilon \approx V_0$. One can understand the physical origin of this feature intuitively by

noting that a positive bias voltage deforms the potential in such a way that the barrier is thinner than it is at zero bias voltage and that a negative bias voltage results in a thicker barrier (see inset of Fig. 1B). Thus, the probability for tunneling at a given $\varepsilon$ below the barrier top is greater for positive bias than for negative bias, such that $\Delta t > 0$ below $\varepsilon \approx V_0$. However, the thinner barrier also tends to be steeper and thus causes more wave reflection for electrons at energies above the barrier, so that $\Delta t < 0$ for $\varepsilon > V_0$. Classically, when the transmission function is simply a sharp step at $\varepsilon = V_0$ (Fig. 3, upper inset), no such sign change occurs.

At around $\varepsilon \approx V_0$, where $\Delta t(\varepsilon)$ changes sign in Fig. 3, the quantum transmission probability is ~0.75 (Fig. 3, upper inset), which corresponds to a linear response conductance of about $G = 1.5e^2/h$ (21). This value agrees well with that of $G$ for the single-barrier R1 at the $V_g$ at which $I_{net}$ changes direction in the measurement at 4 K (Fig. 1B). Similar features are observed in device R10 at about one-sixth the conductance value, a scaling factor that is within the range expected when ballistic transport between neighboring constrictions is considered (25, 26). This agreement between experimental and theoretical data indicates that the positive net current at low $V_g$ is indeed related to tunneling. The qualitative similarity between the two devices shows that any coupling effects between individual ratchet cells do not have a strong effect on the qualitative behavior of the net current. The single-barrier model can therefore also be applied to the periodic ratchet R10. At low temperature (0.4 K), the behavior of the current observed in the experiment is more complex than in the model. The differences may be related to superimposed nonlinear rectifying behavior in the higher 1D subbands that are excluded in the model. Because the effect of

Fig. 3. Theoretical model. The difference $\Delta t(\varepsilon, U_0)$ between the transmission functions for positive and negative voltages for the model potential (Fig. 1B, inset) at $U_0 = 0.5$ mV (bold curve, left axis). Thin curves, energy range $\Delta f(\mu_F, U_0, T)$ where electrons contribute to the current for $\mu_F = 11.7$ meV, $U_0 = 0.5$ mV, and temperatures as indicated (right axis). Sign reversals of $\Delta t$ between 13 and 14 meV are on the resolution limit of the figure. (Upper inset) Quantum mechanical (qm) (solid curve) and classical (cl) (dashed curve) transmission function versus electron energy $\varepsilon$ for $U_0 = 0$. (Lower inset) Net current versus temperature at $\mu_F = 11.7$ meV and rocking voltages $U_0 = 0.3$ mV (dotted curve), 0.5 mV (solid curve), and 0.7 mV (dashed curve).
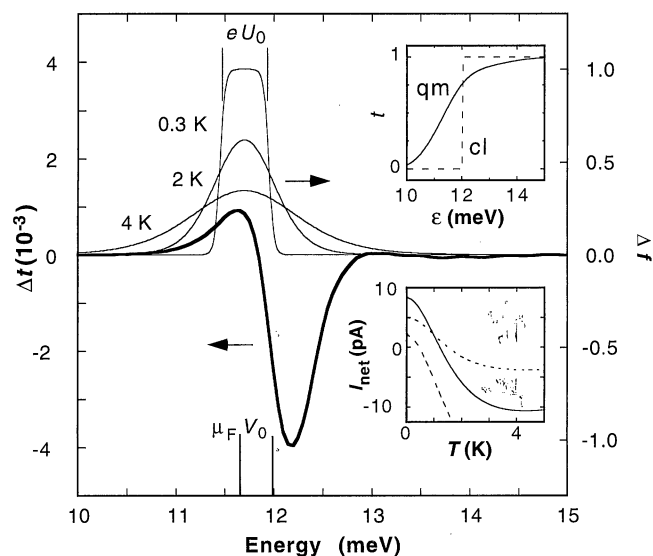
temperature is simply to average $\Delta t(\varepsilon)$ over energy, the more complex behavior of the $I_{net}$ allows us to observe current reversals in both directions in the experiment (Fig. 2A). In close agreement between experiment and model, the temperature at which reversal occurs is typically a few kelvin, a value that is related to the energy scale of variations of $\Delta t(\varepsilon)$ (Fig. 3). The observed $I_{net}$ exceeds that found in the model, indicating that the voltage-induced modification of the ratchet potential is stronger than what is assumed in the calculation. Although a rigorous theoretical treatment will be of interest (24), the 1D single-barrier model used here yields intuitive, qualitative understanding of the sign and temperature dependence of the observed net current.

The observation that the rocking-induced flow of electrons with high and low energy is in opposite directions (Fig. 3) has a fundamentally interesting implication: A tunneling ratchet can perform the energy-sorting task assigned to Maxwell's demon (27), without violating the second law of thermodynamics, because it operates only at a finite voltage. Another important aspect is that artificial nanostructures can be used to test physical principles that may be of importance in living systems. Whether transport mechanisms based on quantum effects such as the one studied here play a role in biological motor proteins is an intriguing question.

**References and Notes**
1. M. O. Magnasco, *Phys. Rev. Lett.* **71**, 1477 (1993).
2. J. Prost, J.-F. Chauwin, L. Peliti, A. Ajdari, *Phys. Rev. Lett.* **72**, 2652 (1994).
3. C. R. Doering, W. Horsthemke, J. Riordan, *Phys. Rev. Lett.* **72**, 2984 (1994).
4. P. Hänggi and R. Bartussek, in *Nonlinear Physics of Complex Systems—Current Status and Future Trends*, J. Parisi, S. C. Müller, W. Zimmermann, Eds. (Springer, Berlin, 1996), pp. 294–308.
5. R. D. Astumian, *Science* **276**, 917 (1997).
6. S. Leibler, *Nature* **370**, 412 (1994).
7. F. Jülicher, A. Ajdari, J. Prost, *Rev. Mod. Phys.* **69**, 1269 (1997).
8. J. Maddox, *Nature* **369**, 181 (1994).
9. K. Kitamura, M. Tokunaga, A. H. Iwane, T. Yanagida, *Nature* **397**, 129 (1999).
10. J. Rousselet, L. Salome, A. Ajdari, J. Prost, *Nature* **370**, 446 (1994).
11. L. P. Faucheux, L. S. Bourdieu, P. D. Kaplan, A. J. Libchaber, *Phys. Rev. Lett.* **74**, 1504 (1995).
12. L. Gorre, E. Ioannidis, P. Silberzan, *Europhys. Lett.* **33**, 267 (1996).
13. H. Linke *et al.*, *Europhys. Lett.* **44**, 341 (1998); H. Linke *et al.*, *Europhys. Lett.* **45**, 406 (1999).
14. A. Lorke *et al.*, *Physica B* **251**, 312 (1998).
15. C. Mennerat-Robilliard *et al.*, *Phys. Rev. Lett.* **82**, 851 (1999).
16. X. Wang, T. Junno, S.-B. Carlsson, C. Thelander, L. Samuelson, available at http://xxx.lanl.gov/abs/cond-mat/9910444.
17. P. Reimann, M. Grifoni, P. Hänggi, *Phys. Rev. Lett.* **79**, 10 (1997).
18. I. Goychuk and P. Hänggi, *Europhys. Lett.* **43**, 503 (1998).
19. P. Hänggi and P. Reimann, *Phys. World* **12**, 21 (March 1999).
20. In addition, to remove any contributions to $I_{net}$ not related to the asymmetry of the device, each experimental sweep was carried out in forward and reverse

configuration of the device, and the two data sets were added.
21. One-dimensional quantum conduction theory is reviewed by S. Datta, *Electronic Transport in Mesoscopic Systems* (Cambridge Univ. Press, Cambridge, 1995).
22. In the sign convention used here, positive electrical current corresponds to an electron particle current in negative *x* direction.
23. H. Xu, *Phys. Rev. B* **47**, 15630 (1993).
24. A rigorous theory of nonlinear quantum transport requires self-consistent treatment of the electrostatic device potential at finite voltage based on the three-dimensional Schrödinger equation.
25. C. W. J. Beenakker and H. van Houten, *Phys. Rev. B* **39**, 10445 (1989).
26. A. A. M. Staring, L. W. Molenkamp, C. W. J. Beenakker, L. P. Kouwenhoven, C. T. Foxon, *Phys. Rev. B* **41**, 8461 (1990).
27. For a collection of key articles, see, for example, H. S. Leff and A. F. Rex, *Maxwell's Demon: Entropy, Information, Computing* (IOP, Bristol, UK, 1990).
28. We acknowledge helpful discussions with P. Reimann, P. Stiles, M. Stopa, O. Sushkov, and H. Xu and technical help by M. Alat, W. D. Sheng, and X. Wang. Supported by the Australian Research Council, the Swedish Research Council for Natural Sciences, the Foundation of Strategic Research, and by a travel grant from the Swedish Institute (A.L.).

# Three-Dimensional Atomic-Scale Imaging of Impurity Segregation to Line Defects

**D. Blavette,\* E. Cadel, A. Fraczkiewicz,† A. Menand**

Clouds of impurity atoms near line defects are believed to affect the plastic deformation of alloys. Three-dimensional atom probe techniques were used to image these so-called Cottrell atmospheres directly. Ordered iron-aluminum alloys (40 atomic percent aluminum) doped with boron (400 atomic parts per million) were investigated on an atomic scale along the ⟨001⟩ direction. A boron enrichment was observed in the vicinity of an ⟨001⟩ edge dislocation. The enriched region appeared as a three-dimensional pipe 5 nanometers in diameter, tangent to the dislocation line. The dislocation was found to be boron-enriched by a factor of 50 (2 atomic percent) relative to the bulk. The local boron enrichment is accompanied by a strong aluminum depletion of 20 atomic percent.

The concept of "atmospheres" was introduced by Cottrell and Bilby (1) in 1949 to explain the role of impurities in the plastic deformation of alloys. These so-called Cottrell atmospheres are tiny clouds of impurity atoms around dislocations in crystals. These line defects play a major role in the plasticity of materials. The geometry of an edge dislocation is described by an extra half-plane inserted into the lattice (Fig. 1). The locus where the half-plane terminates is the dislocation line. Such a dislocation gives rise to an elastic distortion of the lattice around the line of the defect, and consequently to a stress field with which solute impurities may interact. Interstitial impurities such as carbon or boron cause a deformation of the lattice, which may be partially released if these elements segregate near line defects. The stress field created by dislocations is the driving force for the migration of solutes toward dislocations. Interstitial

impurities (or oversized atoms in substitution) generally segregate in the dilated part of edge dislocations, below the dislocation line, whereas undersized substitutional atoms are likely to migrate toward the compressed regions above slip planes. This stress-induced migration therefore leads to the segregation of solutes along dislocation lines and to the formation of solute-enriched regions, the Cottrell atmospheres. Their extent, as estimated from diffusion arguments, is in the nanometer range. Cottrell atmospheres play a major role in the mechanical properties of materials. Their presence may inhibit the movement of dislocations, which are "pinned" by the solute atmospheres. If temperatures are high enough to permit appreciable diffusion, dynamic strain aging may occur during deformation. These so-called Portevin-LeChatelier instabilities are due to the pinning of freshly formed dislocations by new atmospheres that form during deformation. Such dynamic effects have been reported in a number of steels (1).

Direct evidence for these atmospheres is extremely rare because of the very high spatial resolution required. Atom-probe field ion microscopy (APFIM) is the most promising technique for this kind of investigation because it

Sonde Atomique et Microstructures, Groupe de Métallurgie Physique, UMR CNRS 6634, Faculté des Sciences de Rouen, Université de Rouen, 76821 Mont-Saint-Aignan Cedex, France.

\*To whom correspondence should be addressed. E-mail: blavette@univ-rouen.fr
†Ecole des Mines de Saint-Etienne, Centre SMS, 158 Cours Fauriel, 42 100 Saint-Etienne, France.

# LINKED CITATIONS

*- Page 1 of 1 -*

*You have printed the following article:*

**Experimental Tunneling Ratchets**
H. Linke; T. E. Humphrey; A. Lofgren; A. O. Sushkov; R. Newbury; R. P. Taylor; P. Omling
*Science*, New Series, Vol. 286, No. 5448. (Dec. 17, 1999), pp. 2314-2317.
Stable URL:

*This article references the following linked citations:*

## References and Notes

[5] **Thermodynamics and Kinetics of a Brownian Motor**
R. Dean Astumian
*Science*, New Series, Vol. 276, No. 5314. (May 9, 1997), pp. 917-922.
Stable URL:
http://links.jstor.org/sici?sici=0036-8075%2819970509%293%3A276%3A5314%3C917%3ATAKOAB%3E2.0.CO%3B2-N

**NOTE:** *The reference numbering from the original has been maintained in this citation list.*